Volume 32 | Number 2 | February 2017 | Pages 203–422

JAAS

Journal of Analytical Atomic Spectrometry

rsc.li/jaas

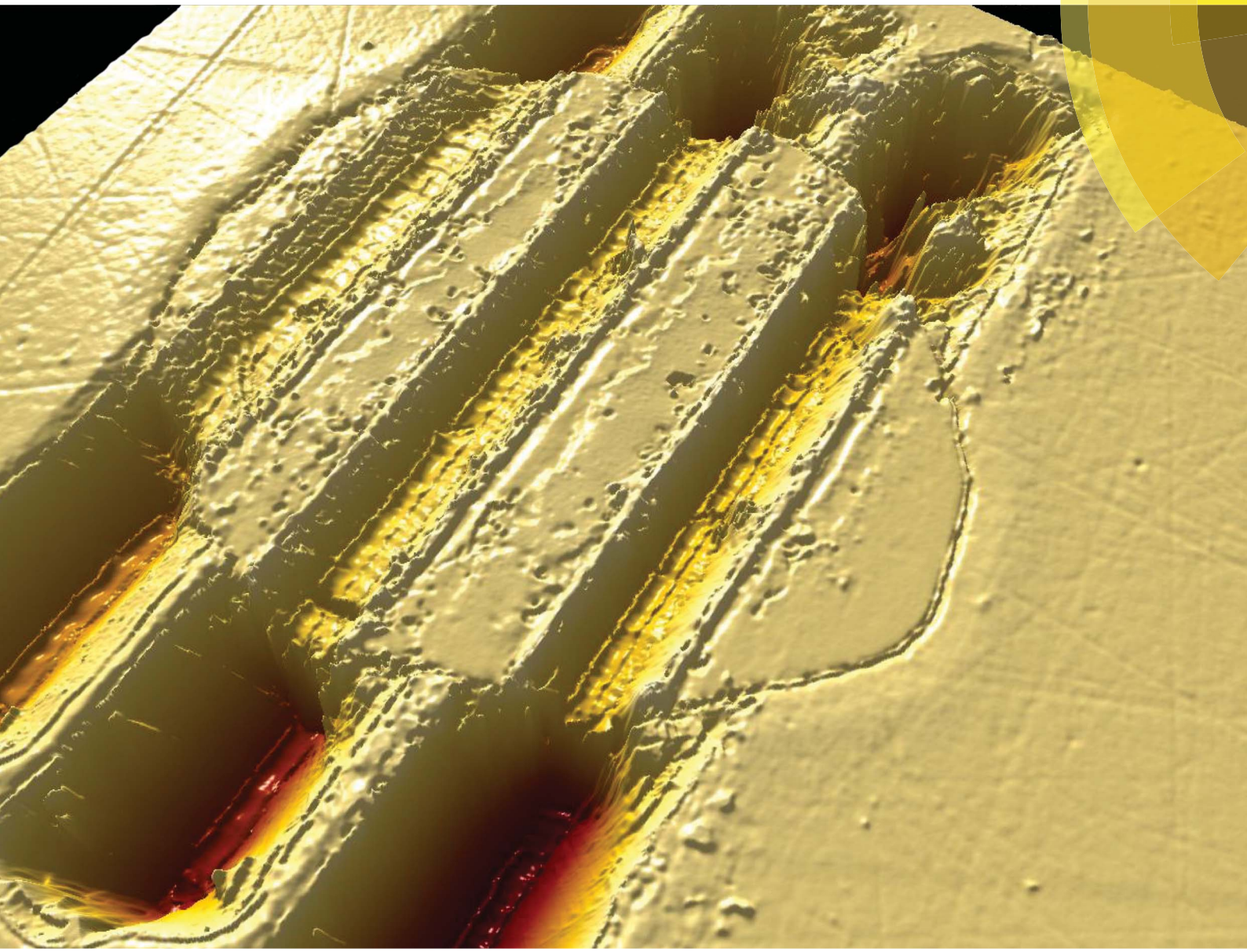

ISSN 0267-9477

ROYAL SOCIETY OF CHEMISTRY

PAPER

David M. Chew *et al.*

Rapid high-resolution U–Pb LA-Q-ICPMS age mapping of zircon

JAAS

PAPER

View Article Online
View Journal | View Issue

Cite this: J. Anal. At. Spectrom., 2017, 32, 262

Rapid high-resolution U–Pb LA-Q-ICPMS age mapping of zircon†

David M. Chew,*[a] Joseph A. Petrus,[b] Gavin G. Kenny[a] and Niall McEvoy[cd]

Zircon commonly exhibits textural evidence for distinct growth events (*e.g.* polyphase core–rim structures) and evidence for Pb mobility not linked to discrete crystallization episodes (Pb loss, incorporation of common Pb, high-temperature Pb mobilization). Interpreting complex U–Pb zircon age data therefore requires imaging of zircon crystals and texturally-controlled sampling to constrain the fine-scale processes affecting the U–Pb zircon systematics. High-resolution U–Pb laser-ablation quadrupole inductively coupled plasma mass spectrometry (LA-Q-ICPMS) zircon age maps were undertaken on zircon sampled from syn-tectonic granitoid suites from the Peruvian Eastern Cordillera that exhibit textural evidence for clearly-defined cores and rims. The images were acquired by rastering a 7 μm spot with a 3.5 J cm^{-2} fluence, with scan speeds of 3 μm s^{-1} and a 10 Hz repetition rate (ThermoScientific iCAP-Qc setup) and scan speeds of 20 μm s^{-1} and a 45 Hz repetition rate (Agilent 7900 system). The mapping-experiment duration for individual zircons was as fast as 10 minutes (Agilent 7900 setup). 91500 zircon was employed as the primary reference material, and secondary-standard data (Temora, Plešovice, WRS-1348, FC-1, Fish Canyon, Tardree) typically reproduce within 1% of their published crystallization ages. Zircon rim concordia ages derived from the U–Pb age maps are consistent with independent secondary ion mass spectrometry (SIMS) and thermal ionisation mass spectrometry (TIMS) constraints. Two-dimensional kernel density estimation of the combined U–Pb data from each map define clear discordia mixing lines between the rim- and core-age components, and also show Pb loss and common Pb vectors. Potential applications of the technique include the characterisation of complex polyphase zircons and characterising the U–Pb systematics of key samples for time-intensive U–Pb TIMS dating.

Received 8th November 2016
Accepted 3rd January 2017

DOI: 10.1039/c6ja00404k

www.rsc.org/jaas

Introduction

The U–Pb zircon system is a very powerful chronometer as it involves two decay schemes (^{235}U–^{207}Pb and ^{238}U–^{206}Pb) which allow for internal consistency assessment of age, a high closure temperature for Pb (>900 °C), and its ability to incorporate moderate amounts of U in its crystal structure yet exclude initial Pb during crystal growth. In addition, the robust physical characteristics of zircon have the potential to preserve chronological information even when the host rock has been metamorphosed, melted, or weathered and eroded away.

However, this ability to preserve multiple events often results in complexities in the U–Pb system within individual zircon grains. For example in magmatic zircons which exhibit textural and geochronological evidence for core–rim structures,[1] the zircon rims are typically linked to late-stage growth corresponding to crystallization from the final pulses of magma (autocrysts), while the cores may represent either zircon antecrysts which crystallized from an earlier pulse of melt in the magma plumbing system, or zircon xenocrysts incorporated from the wall-rocks during magma generation, migration and storage. Similarly, zircon from high-grade metamorphic rocks often exhibits textural and geochronological evidence for core–rim structures,[2] with metamorphic zircon rims typically characterised by a structureless or patchily-zoned appearance in cathodoluminescence (CL) images overgrowing an inherited core.

Additional complexities within the U–Pb zircon system include Pb loss and elevated common Pb contents, both of which induce U–Pb age discordance. Pb loss in zircon is often spatially associated with either high-U domains within the crystal lattice which have accumulated radiation damage by the emission of alpha particles and alpha recoil processes,[3] or zones

[a]Department of Geology, School of Natural Sciences, Trinity College Dublin, Dublin 2, Ireland. E-mail: chewd@tcd.ie

[b]School of Earth Sciences, University of Melbourne, Parkville, Australia. E-mail: jpetrus@unimelb.edu.au

[c]Centre for Research on Adaptive Nanostructures and Nanodevices (CRANN), Advanced Materials Bio-Engineering Research Centre (AMBER), Trinity College Dublin, Dublin 2, Ireland

[d]School of Chemistry, Trinity College Dublin, Dublin 2, Ireland

† Electronic supplementary information (ESI) available. See DOI: 10.1039/c6ja00404k

of crystal-plastic deformation.[4] Common (initial or non-radiogenic) Pb can only be incorporated in the zircon crystal lattice in very small amounts, and most of the common Pb in zircon is likely hosted in inclusions and in microscopic alteration zones connected *via* cracks to the grain exterior.[5] It was also hypothesized that radiogenic Pb in zircon is tetravalent and compatible in zircon, with a diffusivity 3–4 orders of magnitude lower than that of divalent Pb (the assumed valence state of common Pb). A tetravalent state for radiogenic Pb would account for the extreme retentivity of the zircon U–Pb system at high temperatures, and the observation that in both zircon evaporation and zircon leaching experiments, common Pb is generally released preferentially to radiogenic Pb.[5]

Hence as zircon can exhibit both distinct growth events (polyphase core–rim structures) and evidence for Pb mobility not linked to discrete crystallization episodes (Pb loss, incorporation of common Pb and Pb mobilization at high temperatures) and these are usually recorded in micron- to few tens of micron-scale structures, the correct interpretation of U–Pb zircon age data requires elemental and isotopic imaging of zircon crystals and subsequent texturally-controlled sampling in order to understand the processes that affect the U–Pb age, chemistry and/or internal structure of zircon at an appropriate scale. In U–Pb zircon dating studies, cathodoluminescence (CL) and back-scattered electron (BSE) are the most commonly employed imaging methods. However, while CL often gives qualitative constraints on the degree of complexity of the growth structures, it should be noted that distinct boundaries between CL zones do not always correlate with detectable age differences within a grain, or domains which have experienced Pb mobility.[6]

Other imaging techniques are being increasingly applied to U–Pb zircon studies, including electron back-scattered diffraction[4] (EBSD) and secondary ion mass spectrometry (SIMS) ion imaging.[7] In addition to producing U–Pb and Pb–Pb age and element maps with micron-scale spatial resolution, SIMS scanning ion imaging studies have also documented the occurrence of micrometre-scale clusters of unsupported radiogenic Pb in ultra-high temperature (UHT) metamorphic zircon,[8] where it likely results from annealing of radiation-damaged zircon. Atom probe tomography shows that radiogenic Pb clusters in zircon can also be composed of isolated nanoclusters, measuring about 10 nm and spaced 10–50 nm apart.[9]

Laser ablation inductively coupled plasma mass spectrometry (LA-ICPMS) is now the most commonly-used analytical method in U–Pb zircon dating studies, primarily due to the widespread availability of LA-ICPMS systems and the speed of data acquisition. Analysis durations as short as 30 seconds with spot sizes as small as 25 μm in diameter are now routinely used in U–Pb zircon dating studies,[6] and will likely decrease further with ever-increasing technological improvements in laser as well as ICP-MS instrumentation. Although LA-ICPMS U–Pb zircon dating depth-profiling studies can reveal age and simultaneous trace-element information on the micron-scale,[10–12] it is difficult to spatially link these depth-profiling data with textural surface images. This study combines zircon CL and Raman imaging[13] with rapid high-spatial resolution LA-ICPMS mapping of U–Pb age and elemental information (U and Th abundances and Th/U ratios), to characterise how compositional and structural variation information within zircon crystals is related to age.

Samples–field relationships and zircon petrography

The samples investigated in this study (samples DC 04/5-2 and DC 05/5/7) were collected from the Eastern Cordillera of Peru, which comprises a series of Paleozoic metasedimentary rocks intruded by several Paleozoic syn- and post-tectonic granitoid suites.[14] The samples were selected as the zircon grain size is typical of coarse crystalline basement rocks (grain sizes of between 100 × 50 μm^2 to 200 × 100 μm^2), and they exhibit textural evidence for clearly defined cores and rims, which is backed up by *in situ* U–Pb SIMS and LA-ICPMS geochronology.[15]

Sample DC 04/5-2

Sample DC 04/5-2 is a strongly-foliated granodiorite (the *Sitabamba orthogneiss*[15]), with conspicuous augen of relic igneous plagioclase and the development of metamorphic biotite and garnet. The *Sitabamba orthogneiss* locally intrudes high-grade Paleozoic schists of the Marañon Complex. Thermobarometric estimates for the peak metamorphic conditions are 700 °C and 12 kbar,[16] but with no evidence for anatexis in the adjacent Marañon Complex country rock. The crystallization of the granodioritic protolith has been constrained by a U–Pb TIMS zircon concordia age of 442.4 ± 1.4 Ma and a LA-ICPMS U–Pb zircon concordia age of 444.2 ± 6.4 Ma.[15] Titanite and apatite from the same sample yield U–Pb Tera–Wasserburg concordia lower intercept ages of 437.1 ± 5.3 and 365 ± 14 Ma respectively[17] which record post-emplacement cooling. U–Pb LA-ICPMS dating of xenocrystic zircon cores within the *Sitabamba orthogneiss* range from 0.5 to 0.7 Ga and 0.9 Ga to 2.1 Ga, with prominent peaks at 0.6 and 1.1 Ga (sample DC 04/5-2).[15]

Sample DC 04/5-2 yielded one population of prismatic, euhedral zircons with aspect ratios of *ca.* 2 : 1, and ranging between 100 and 200 μm in length. The grains show prominent oscillatory, idiomorphic zoning in CL.[15] Approximately 50% of the grains yield textural evidence for small, equant cores, which are typically 50 μm in diameter. These cores also show oscillatory zoning, which is usually sharply truncated at the core–rim boundary (*e.g.* Fig. 6A and 7A). The CL response of both the core and rim regions is similar and is indicative of a magmatic origin for both the rims and the xenocrystic cores. Th/U ratios of the magmatic rims of the *Sitabamba orthogneiss* typically range between 0.1 and 0.4.[15]

Sample DC 05/5-7

Sample DC 05/5-7 was collected 100 km to the north of sample DC 04/5-2. Here the Marañon Complex is of higher metamorphic grade, and comprises biotite-garnet paragneisses intruded by a series of leucocratic layers that share the same foliation as the country rock. Sample DC 05/5-7 was taken from a thick, foliated leucocratic layer (5 m across). The zircon rims have yielded a U–Pb SIMS concordia zircon age of 477.9 ± 4.3 Ma,[15]

which constrains the crystallization of the leucocratic melt. LA-ICPMS dating of detrital zircons from the adjacent paragneiss country rock have yielded U–Pb age spectra which range from 0.7 to 1.7 Ga, with a prominent peak at 1.1 Ga (sample DC 05/5-4).[15]

Sample DC 05/5-7 yielded an extremely diverse population of zircons. The majority of the population is composed of large (often up to 200 μm in diameter) faceted grains (which were either long prismatic, short prismatic, or sub-spherical in habit, with a discrete subpopulation of small prismatic, euhedral zircons that rarely exceeded 100 μm in length). Under CL, the distinction between the two subpopulations is clear.[15] The small euhedral prisms are CL dark and have faint idiomorphic zoning with rare inherited cores. The coarser grains are the subpopulation examined in this study, and typically exhibit a thin (10–30 μm) CL dark rim with faint idiomorphic zoning, which surrounds a large inherited core that makes up the majority of the zircon crystal (*e.g.* Fig. 3A, 4A and 5A). The inherited cores exhibit a wide variety of forms, zoning patterns, and CL intensities, which reflect the variable nature of the precursor detrital zircon population. The previously published U–Pb SIMS concordia age of 477.9 ± 4.3 Ma (ref. 15) was obtained from the CL dark rims, while one inherited core has yielded a $^{206}Pb/^{238}U$ SIMS age of 1093 ± 16 Ma. Th/U ratios of the zircon rims were typically extremely low, averaging around 0.05.[15]

Cathodoluminescence and Raman imaging analytical technique

Both samples were mounted in 25 mm diameter epoxy mounts and the grains were ground and polished to half-thickness to expose the grain interiors. The mounts were then coated with a *ca.* 10 nm-thick layer of carbon and the zircons imaged by cathodoluminescence (CL) using a KE Developments Centaurus system attached to a Tescan Mira XMU Field Emission Scanning Electron Microscope (SEM) at the Centre for Microscopy and Analysis (CMA) at Trinity College, Dublin. An accelerating voltage of 10 kV and working distance of *ca.* 10 mm were employed. CL imaging was undertaken immediately prior to all LA-ICPMS imaging experiments. Following an imaging experiment, the sample was polished down by approximately 5 microns with a Struers LaboPol 21 automated polisher using 6 μm and then 1 μm diamond suspension fluids.

Zircon laser Raman spectroscopy maps were performed at Trinity College Dublin's Centre for Research on Adaptive Nanostructures and Nanodevices (CRANN) using a WITec Alpha 300 R microscope with a 20× objective (numerical aperture of 0.4). Raman peak intensity maps were undertaken on the same grains imaged by CL. An excitation wavelength of 532 nm, with 5 mW laser power, and an 1800 grooves per mm grating were used. The instrument spectral resolution (a measure of the ability to resolve spectral features and bands into their separate components) was *ca.* 1 cm^{-1}. The pixel size on the Raman maps is 1 μm^2 (*i.e.* a 100 × 100 μm area consists of 10 000 individual spectra), and the collection time for each zircon map was approximately 20 minutes. Raman peak intensity maps are presented for all samples at the 1005.5 cm^{-1} band, and for some samples at the 439.8 cm^{-1} band. The Raman peak intensity maps were acquired following the iCAP Qc LA-ICPMS mapping experiments and prior to the Agilent 7900 LA-ICPMS mapping experiments which are described below. The CL and Raman images and LA-ICPMS maps from the Agilent 7900 experiments are presented in Fig. 3–7; the corresponding maps from the iCAP Qc experiments are presented in the ESI (Fig. 1–5).† The same Raman maps are presented with the LA-ICPMS images from both analytical setups.

LA-ICPMS imaging analytical technique

LA-ICPMS elemental and U–Pb age image maps were acquired using a Photon Machines Analyte Excite 193 nm ArF excimer laser-ablation system with a Helex 2-volume ablation cell coupled initially to a Thermo Scientific iCAP Qc, and subsequently (following repolishing and CL and Raman imaging) to an Agilent 7900 ICPMS at the Department of Geology, Trinity College Dublin. Both ICPMS instruments were tuned using NIST612 standard glass to yield Th/U ratios of unity and low oxide production rates (ThO^+/Th^+ typically <0.15%). Two and three zircon grains were imaged from samples DC 04/5-2 (grains 809, 812) and DC 05/5-7 (grains 820, 822 and 823) respectively.

For the iCAP Qc experiments, 0.65 l min^{-1} He carrier gas was split evenly between the large outer sample chamber and the small inner volume (the "cup") where ablation occurs. An in-house developed variable-volume signal-smoothing device was used to mix the He aerosol with 0.7 l min^{-1} Ar make-up gas and a small

Table 1 Analytical parameters for different sessions

Laser parameters	
Instrument	Photon Machines Analyte Excite ArF Excimer 193 nm
Washout and background	10 or 25[a] s
Laser repetition rate	10[a] or 45 Hz
Spot size	7 or 10 micron diameter
Energy	3.5 J cm^{-2}
Laser carrier gas	0.65[a] or 0.7 L min^{-1} He
Mass spectrometer parameters	
Instrument	Thermo Scientific iCAP Qc
Plasma RF power	1450 W
Plasma carrier gas flow	0.7 L min^{-1}
Isotopes measured with dwell times [ms] listed[b]	^{91}Zr [5], ^{204}Pb [10], ^{206}Pb [60], ^{207}Pb [75], ^{208}Pb [20], ^{232}Th [10], ^{238}U [30]
Total duty cycle	210 ms
Instrument	Agilent 7900
Plasma RF power	1500 W
Plasma carrier gas flow	0.56 L min^{-1}
Isotopes measured with dwell times [ms] listed	^{90}Zr [1.3], ^{204}Pb [2], ^{206}Pb [12], ^{207}Pb [15], ^{208}Pb [4], ^{232}Th [2], ^{238}U [6]
Total duty cycle	58.3 ms

[a] Parameters used for analytical sessions on the iCAP Qc. [b] iCAP Qc dwell times also incorporate scanning/settling time.

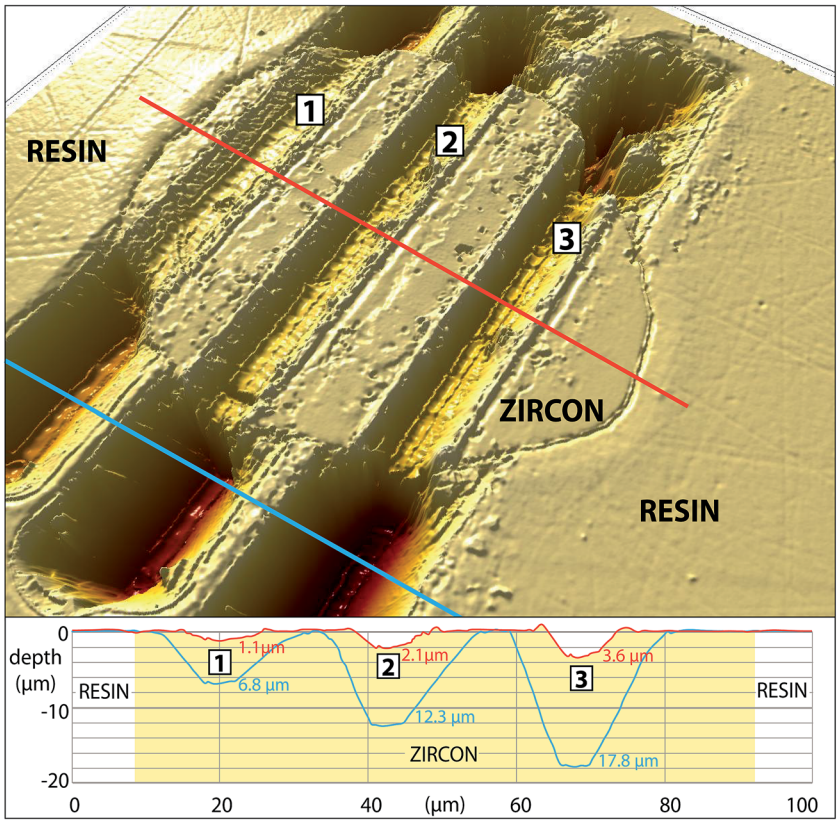

Fig. 1 White light interferometry 3D image with corresponding 2D profiles from a representative zircon from sample DC 05/5-7 ablated using the same laser conditions as the Agilent 7900 experiments. The numbers in boxes (1, 2, 3) correspond to the number of successive ablation passes. The 2D profiles record the depths through the ablated zircon (red profile) and the adjacent epoxy resin (blue profile).

volume of N_2 (*ca.* 6 ml min^{-1}) to enhance signal sensitivity and reduce oxide formation (Table 1). The Analyte Excite – iCAP Qc setup yields a washout with 90% signal reduction in less than 1.5 s. For the Agilent 7900 experiments, 0.5 l min^{-1} He carrier gas was fed into the cell body and 0.2 l min^{-1} He was fed into the cup, and the aerosol was subsequently mixed with 0.56 l min^{-1} Ar make-up gas and 6 ml min^{-1} of N_2. The Ar and N_2 were added in a *ca.* 1 cm^3 mixing bulb resulting in a significantly faster washout for image mapping experiments on the Agilent 7900 (90% signal reduction in less than 0.25 s), and consequently higher laser scan speeds and repetition rates and shorter duty cycles could be employed.

Seven isotopes (^{90}Zr or ^{91}Zr, ^{204}Pb, ^{206}Pb, ^{207}Pb, ^{208}Pb, ^{232}Th and ^{238}U) were acquired using a fluence of *ca.* 3.5 J cm^{-2} with a total duty cycle of 210 ms (iCAP Qc) or 58.3 ms (Agilent 7900) (Table 1). All Agilent 7900 experiments employed a 7 μm diameter circular spot, while either a 7 or 10 μm diameter circular spot was used for the iCAP Qc experiments (it should be noted that the smallest square spot on our Analyte Excite system is 12 μm across). The pulse energy is set comfortably above (*ca.* 20%) the ablation threshold for NIST612 glass and zircon on our LA-ICPMS system, yet not set too high so as to reduce the effects of melting on the crater walls which can cause fractional evaporation of volatile elements.[18] The combination of laser repetition rate and laser scan speeds (3 or 4 μm s^{-1} and 10 Hz laser repetition rate on the iCAP Qc; 20 μm s^{-1} and 45 Hz laser repetition rate on the Agilent 7900, Tables 1 and 3) were chosen as to yield relatively shallow pit diameter/depth ratios, which minimizes downhole-fractionation of U–Pb.[19] Measurement of raster pit profiles on one representative zircon from sample DC 05/5-7 was carried out using an Omniscan MicroXan White Light Interferometer. This technique measures surface roughness and texture and is capable of rapid 3D scanning to capture data for off-line plotting and visualization. The optical interferometry 3D image and corresponding 2D profiles from this zircon are presented in Fig. 1, and show that one raster line (using the same laser conditions as in the Agilent 7900 experiments) removes 1.1 μm of material from the zircon surface; it also demonstrates the raster trenches are approximately six times deeper when they pass into the adjacent epoxy resin.

U–Pb data reduction and image processing using Iolite

Image maps were made by "rastering" the sample under the ablation site, similar to earlier trace element image-mapping protocols from our laboratory.[20] To produce the full map, adjacent lines (or "rasters") were ablated in a successive manner. The final ablated area was rectangle-shaped as it simplifies the production of U–Pb and trace-element maps using our data

Table 2 U–Pb zircon ages for secondary standards

	Temora	MSWD	*n*	Plešovice	MSWD	*n*	WRS 1348	MSWD	*n*	FC-1	MSWD	*n*	Fish Canyon	MSWD	*n*	Tardree	MSWD	*n*
Age from literature	*416.8 ± 1.3 Ma*			*337.13 ± 0.37 Ma*			*526.26 ± 0.70 Ma*			*1099.0 ± 0.6 Ma*			*28.37 ± 0.05 Ma*			*61.32 ± 0.09 Ma*		
Session #1 (iCAP)	420.7 ± 8.1 Ma	0.96	13	—	—	—	—	—	—	—	—	—	—	—	—	—	—	—
Session #2 (iCAP)	423.7 ± 4.2 Ma	0.92	15	—	—	—	—	—	—	—	—	—	—	—	—	—	—	—
Session #3 (iCAP)	419.1 ± 3.8 Ma	1.12	12	—	—	—	—	—	—	—	—	—	—	—	—	—	—	—
Session #4 (Agilent)	410.6 ± 4.3 Ma	0.97	8	338.9 ± 1.5 Ma	0.61	10	529.7 ± 3.6 Ma	0.82	15	1109.6 ± 5.0 Ma	1.6	12	—	—	—	—	—	—
Session #5 (Agilent)	414.9 ± 3.2 Ma	0.82	8	339.1 ± 2.1 Ma	0.88	11	530.4 ± 2.6 Ma	1.06	15	—	—	—	—	—	—	—	—	—
Session #6 (Agilent)	419.8 ± 3.0 Ma	0.33	7	335.7 ± 3.9 Ma	1.7	10	523.2 ± 3.3 Ma	1.5	11	—	—	—	—	—	—	—	—	—
Session #7 (Agilent)	420.5 ± 7.0 Ma	2.6	7	334.5 ± 3.8 Ma	2.3	10	528.1 ± 3.3 Ma	1.9	15	—	—	—	—	—	—	—	—	—
Session #8 (Agilent)	—	—	—	—	—	—	530.5 ± 6.3 Ma	0.86	6	—	—	—	28.36 ± 0.41 Ma	0.56	21	60.97 ± 0.88 Ma	0.47	10
Session #9 (Agilent)	—	—	—	334.9 ± 4.1 Ma	0.74	14	—	—	—	—	—	—	—	—	—	—	—	—
Agilent wtd. average	*416.4 ± 6.6 Ma*			*338.1 ± 2.3 Ma*			*528.3 ± 3.0 Ma*											

reduction protocol described later. Twenty-five seconds were allowed for washout between lines to avoid any carry-over from standards to samples and *vice versa* on the Analyte Excite – iCAP Qc setup; the more rapid washout on the Analyte Excite – Agilent 7900 system enabled a faster washout of 10 seconds to be employed. The latter 50% of the washout signal was used for baseline measurements on both setups.

The 91500 zircon ($^{206}Pb/^{238}U$ TIMS age of 1065.4 ± 0.6 Ma (ref. 21)) was used as the primary U–Pb and trace-element calibration standard (80.0 ppm U, 29.9 ppm Th and 14.9 ppm Pb LA-ICPMS values[22]), and ablated with the same parameters as the sample rasters. NIST612 glass and Temora 2 zircon ($^{206}Pb/^{238}U$ TIMS age of 416.8 ± 1.3 Ma (ref. 23)) were used as the secondary U–Pb and trace-element calibration standards respectively in the majority of experiments on the iCAP Qc and Agilent 7900 (Table 2). Additionally, Plešovice zircon ($^{206}Pb/^{238}U$ TIMS age of 337.13 ± 0.37 Ma and LA-ICPMS abundance determinations of 755 ppm U and 78 ppm Th[24]) and WRS 1348 zircon ($^{206}Pb/^{238}U$ TIMS age of 526.26 ± 0.70 Ma and 73 ± 13 ppm U (ref. 25)) were analysed in most Agilent 7900 experiments (Table 2). FC-1 zircon ($^{207}Pb/^{206}Pb$ TIMS age of 1099.0 ± 0.6 Ma (ref. 26)), Fish Canyon zircon ($^{206}Pb/^{238}U$ TIMS age of 28.37 ± 0.05 Ma (ref. 27)) and Tardree zircon ($^{206}Pb/^{238}U$ TIMS age of 61.32 ± 0.09 Ma (ref. 28)) were analysed each in one Agilent 7900 experiment (Table 2).

Typically two NIST612, three 91500 zircon and two or three Temora 2 traverses were analysed at the beginning and end of each zircon mapping experiment on both setups. Three traverses of Plešovice and WRS 1348 zircon were also analysed at the beginning and end of each zircon mapping experiment in most Agilent 7900 sessions, along with one session that included FC-1 zircon and one session that included Fish Canyon and Tardree zircon (Table 2). The duration of each individual zircon mapping experiment typically took between 23 and 44 minutes on the iCAP Qc and between 10 and 23 minutes on the Agilent 7900 (Table 3). It should be noted that the rapidity of the Agilent 7900 mapping experiments facilitated a conservatively large mapped area and the images were subsequently cropped to produce an area of interest slightly larger than the zircon crystal. All of the Agilent 7900 mapping experiments (with the exception of grain 823 from sample DC 05/5-7) could have been mapped in less than 10 minutes using a smaller raster area.

Data reduction and production of U–Pb and trace-element distribution maps was undertaken using Iolite[29] (v3.4), a software package developed for mass spectrometric data reduction. It was developed as a set of procedures for Igor Pro (http://www.wavemetrics.com), a relatively inexpensive platform for scientific graphing, data analysis and image processing of time series data. Iolite is capable of processing very large datasets (*e.g.* multi-hour sessions of laser ablation data) with a strong emphasis on viewing and editing data in graphical form as plots of signal intensity, isotopic ratios or elemental ratios *vs.* time. U–Pb data reduction was undertaken using the "VizualAge"[29] data reduction scheme (DRS) which is itself based on the earlier "U–Pb Geochronology" data reduction scheme.[31] Long rasters (between 400 and 900 μm) were undertaken on the 91500 zircon U–Pb primary reference material. No U–Pb downhole fractionation correction was applied in VizualAge. Following data reduction using the "VizualAge" DRS, U–Pb age and trace-element distribution maps were built using the Iolite module "Images from Selections". The majority of image and age maps were acquired using a 7 μm spot diameter. For the iCAP Qc experiments (duty cycle of 210 ms and a typical scan speed of 3 μm s^{-1}, Tables 1 and 3), each pixel on the images has dimensions of 7 μm × 0.63 μm [±3.5 μm]. The duty cycle of 58.3 ms and scan speed of 20 μm s^{-1} on the Agilent 7900 experiments (Table 1) results in pixel dimensions of 7 μm × 1.16 μm [±3.5 μm].

Concordia ages were calculated for zircon from samples DC 04/5-2 and DC 05/5/7 by manually selecting concordant segments of the line rasters using the "Live Concordia" function of the "VizualAge".[30] This was undertaken by using the $^{206}Pb/^{238}U$ age and the Th/U ratio channels as monitors to help guide selection of portions of the line rasters. These segments of the line raster signals were then adjusted manually using the "Live Concordia" function, so that only concordant portions were selected on the zircon rims and cores. The cores of zircons 823 and 820 from sample DC 05/5-7 yielded an almost continuous discordia mixing line between the maximum core age and

Table 3 U–Pb zircon ages for selected domains from the zircon image maps

Sample	Zircon #	Session ID	Duty cycle	# of scans	Duration	Spot size	Rep. rate	Scan speed	Rim Conc. age	MSWD	*n*	Core Conc. age	MSWD	*n*
DC 05/5-7	823	1 (iCAP)	210 ms	43	43′04	10 μm	10 Hz	4 μm s^{-1}	484.4 ± 8.1 Ma	0.97	7	1111 ± 8.3 Ma	1.2	17
DC 05/5-7	822	2 (iCAP)	210 ms	21	22′55	10 μm	10 Hz	4 μm s^{-1}	475.7 ± 6.6 Ma	1.5	10	1178 ± 24 Ma	0.84	6
DC 05/5-7	820	3 (iCAP)	210 ms	26	44′09	7 μm	10 Hz	3 μm s^{-1}	458.8 ± 6.8 Ma	1.7	7	1056 ± 14 Ma	0.94	11
DC 04/5-2	809	3 (iCAP)	210 ms	32	39′02	7 μm	10 Hz	3 μm s^{-1}	440.0 ± 4.2 Ma	1.8	20	618 ± 11 Ma	1.06	8
DC 04/5-2	812	3 (iCAP)	210 ms	23	31′20	7 μm	10 Hz	3 μm s^{-1}	436.8 ± 5.5 Ma	1.9	18	1808 ± 21 Ma	0.54	5
DC 05/5-7	823	5 (Agilent)	58.3 ms	49	22′48	7 μm	45 Hz	20 μm s^{-1}	477.0 ± 9.8 Ma	2.1	11	1133 ± 12 Ma	1.6	13
DC 05/5-7	822	8 (Agilent)	58.3 ms	33	11′56	7 μm	45 Hz	20 μm s^{-1}	475.5 ± 3.9 Ma	1.17	18	1197 ± 12 Ma	0.61	9
DC 05/5-7	820	9 (Agilent)	58.3 ms	49	18′41	7 μm	45 Hz	20 μm s^{-1}	480.5 ± 5.6 Ma	0.73	19	1052 ± 27 Ma	1.08	5
DC 04/5-2	809	6 (Agilent)	58.3 ms	34	10′56	7 μm	45 Hz	20 μm s^{-1}	442.8 ± 5.8 Ma	0.64	17	606 ± 22 Ma	2.4	7
DC 04/5-2	812	6 (Agilent)	58.3 ms	37	12′42	7 μm	45 Hz	20 μm s^{-1}	436.5 ± 8.5 Ma	0.55	9	1708 ± 16 Ma	1.3	8
DC 04/5-2	All rims weighted average (Agilent)								*440.8 ± 4.8 Ma*					
DC 05/5-7	All rims weighted average (Agilent)								*477.1 ± 3.0 Ma*					

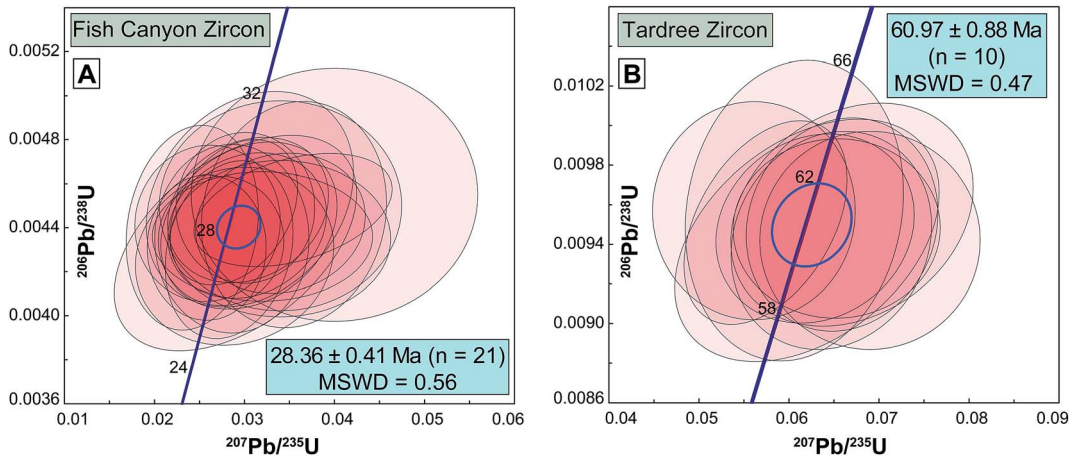

Fig. 2 Representative concordia ages for Fish Canyon Tuff and Tardree zircon from one Agilent 7900 session. Both concordia ages are derived from raster segments from one individual zircon crystal.

the rim crystallization age (Fig. 5I and K); in this case the oldest concordant segments of the core were selected. The concordant portions of the line rasters were then overlain over the U–Pb image maps so that they can be spatially related and compared with the CL and Raman intensity maps. The final concordia age calculations of both the U–Pb zircon secondary age standard and segments of the line raster unknowns were undertaken using Isoplot 4.15.[32] The MSWD of the U–Pb concordia age calculation employs both the MSWD for X–Y equivalence and the MSWD for concordance.

To further characterize the U–Pb systematics of the imaged zircons, two-dimensional kernel density estimates created from individual image data points in the Wetherill concordia space were constructed (*cf.* Fig. 3I, 4J, 5K, 6J and 7J). To do so, the Igor Pro packed experiment files saved by Iolite were exported *via* the "Igor" package, allowing the raw image data to be manipulated and processed as matrices using an in-house program written in the Python programming language. The image matrices were trimmed to include only data corresponding to a certain threshold Zr count rate (~20 Mcps) and also to exclude undefined data, *i.e.*, those that involve division by zero, which may occur near the grain boundary where the U signal drops off rapidly. Two-dimensional kernel density estimates were constructed from these refined datasets with the "seaborn" Python package (a Python visualization library) using a Gaussian kernel and the bandwidth as determined by "Scott's rule".[33]

Results

Secondary age standard data

Prior to the U–Pb imaging mapping experiments, initial developmental work employing high spatial resolution (7 or 10 μm) rasters focussed on accurately reproducing the age of secondary zircon reference materials using 91500 zircon as a primary age standard. Some preliminary experiments on the iCAP Qc setup exhibited a difference in ablation behavior (*e.g.* Zr signal intensity and/or U–Pb fractionation) between 91500 zircon and the secondary zircon reference materials. Careful monitoring of the focus on the laser ablation system (to correct for minor drift on the *z*-axis of the sample stage), tuning the LA-ICPMS system on NIST 612 standard glass to yield Th/U ratios of unity, and an optimal choice of pulse energy was found to improve the age reproducibility of the secondary standards (Table 1 and Fig. 2).

All secondary standard age data (U–Pb concordia ages from individual sessions) reproduce within 1% of their published crystallization ages (Table 2), with the exception of the Temora 2 data from session #2 on the iCAP Qc (423.7 ± 4.2 Ma; +1.66%) and session #4 on the Agilent 7900 (410.6 ± 4.3 Ma; −1.49%). The weighted average data of the U–Pb concordia ages from the Agilent sessions (Table 2) show that Temora 2 (416.4 ± 6.6 Ma), Plešovice (338.1 ± 2.3 Ma) and WRS 1348 (528.3 ± 3.0 Ma) zircon all reproduce within 0.5% of their published crystallization ages (416.8 ± 1.3 Ma, 337.13 ± 0.37 Ma and 526.26 ± 0.70 Ma respectively). Representative concordia ages for Fish Canyon Tuff and Tardree zircon from one Agilent 7900 session (session 8, Table 2) are presented in Fig. 2. These concordia ages are both from a single grain, and demonstrate the degree of precision and accuracy that can be achieved on young (Cenozoic) grains using 7 μm rasters. All U–Pb zircon raster data (isotopic ratios and ages) for the Agilent 7900 and iCAP-Qc experiments are presented in Table 1 of the ESI.†

Comparison of the LA-ICPMS, CL and Raman images

Zircons from the leucocratic sheet sample DC 05/5-7 (grains 823, 822 and 820, Fig. 3–5) exhibit thin (10–30 μm) CL dark rims with faint idiomorphic zoning, which surround a large inherited magmatic core with a bright, zoned CL response that makes up the majority of the zircon crystal. There is a clear correlation between the LA-ICPMS U concentration maps and the CL images in Fig. 3–5 (CL dark = high U; CL bright = low U), while the Raman peak intensity maps also identify clear core–rim relationships and additional internal structure at the 1005.5 cm^{-1} band (Fig. 3G and 5H) or the 439.8 cm^{-1} band (Fig. 4G). The Th/U ratio maps for sample DC 05/5-7 also help identify core–rim structures. The zircon rims on the CL images are

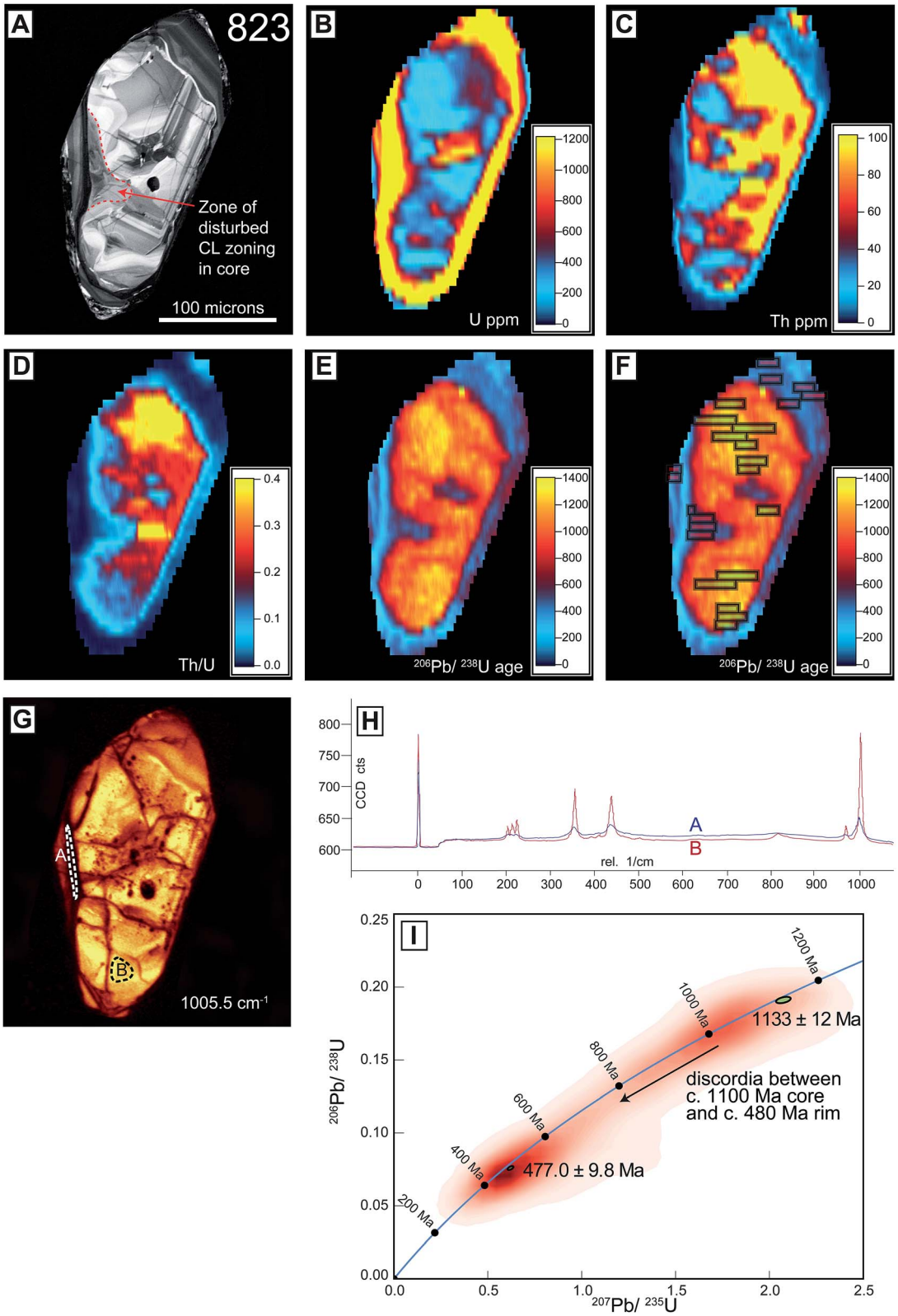

Fig. 3 Zircon 823 from leucocratic sheet sample DC 05/5-7. (A) CL image. (B–E) Agilent 7900 LA-ICPMS U ppm, Th ppm, Th/U ratio and $^{206}Pb/^{238}U$ image maps. (F) $^{206}Pb/^{238}U$ image map with concordant portions of the U/Pb signal denoted. (G) Raman peak intensity map at the 1005.5 cm^{-1} band. (H) Raman spectra of a representative metamict subdomain (trace A) and crystalline subdomain (trace B) from this sample. (I) Two-dimensional kernel density estimates from individual image data points plotted in the Wetherill concordia space. The concordia ages are calculated from the concordant portions of the U/Pb signal marked on (F).

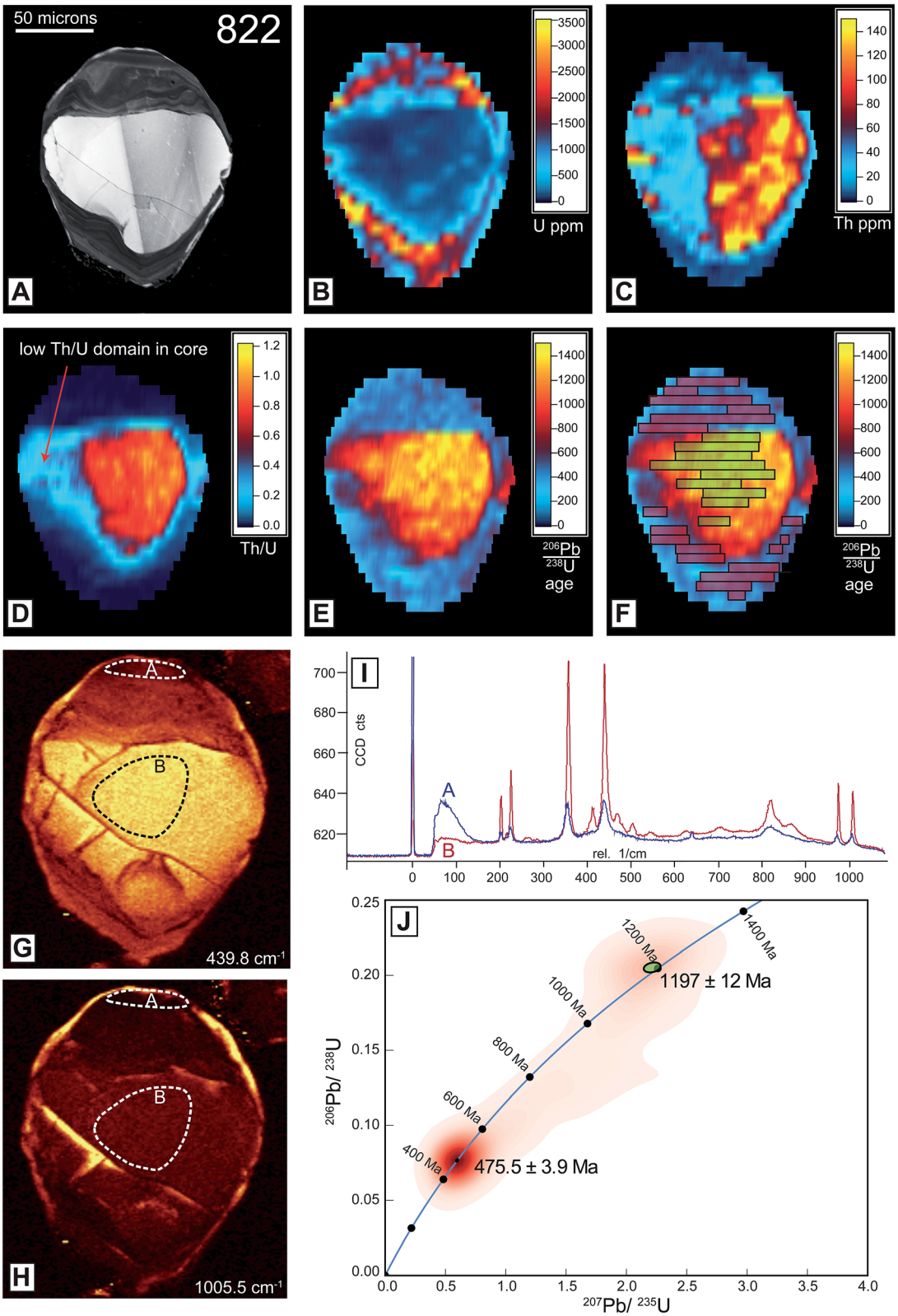

Fig. 4 Zircon 822 from leucocratic sheet sample DC 05/5-7. (A) CL image. (B–E) Agilent 7900 LA-ICPMS U ppm, Th ppm, Th/U ratio and $^{206}Pb/^{238}U$ image maps. (F) $^{206}Pb/^{238}U$ image map with concordant portions of the U/Pb signal denoted. (G and H) Raman peak intensity maps at the 439.8 cm^{-1} and 1005.5 cm^{-1} bands. (I) Raman spectra of a representative metamict subdomain (trace A) and crystalline subdomain (trace B) from this sample. (J) Two-dimensional kernel density estimates from individual image data points plotted in the Wetherill concordia space. The concordia ages are calculated from the concordant portions of the U/Pb signal marked on (F).

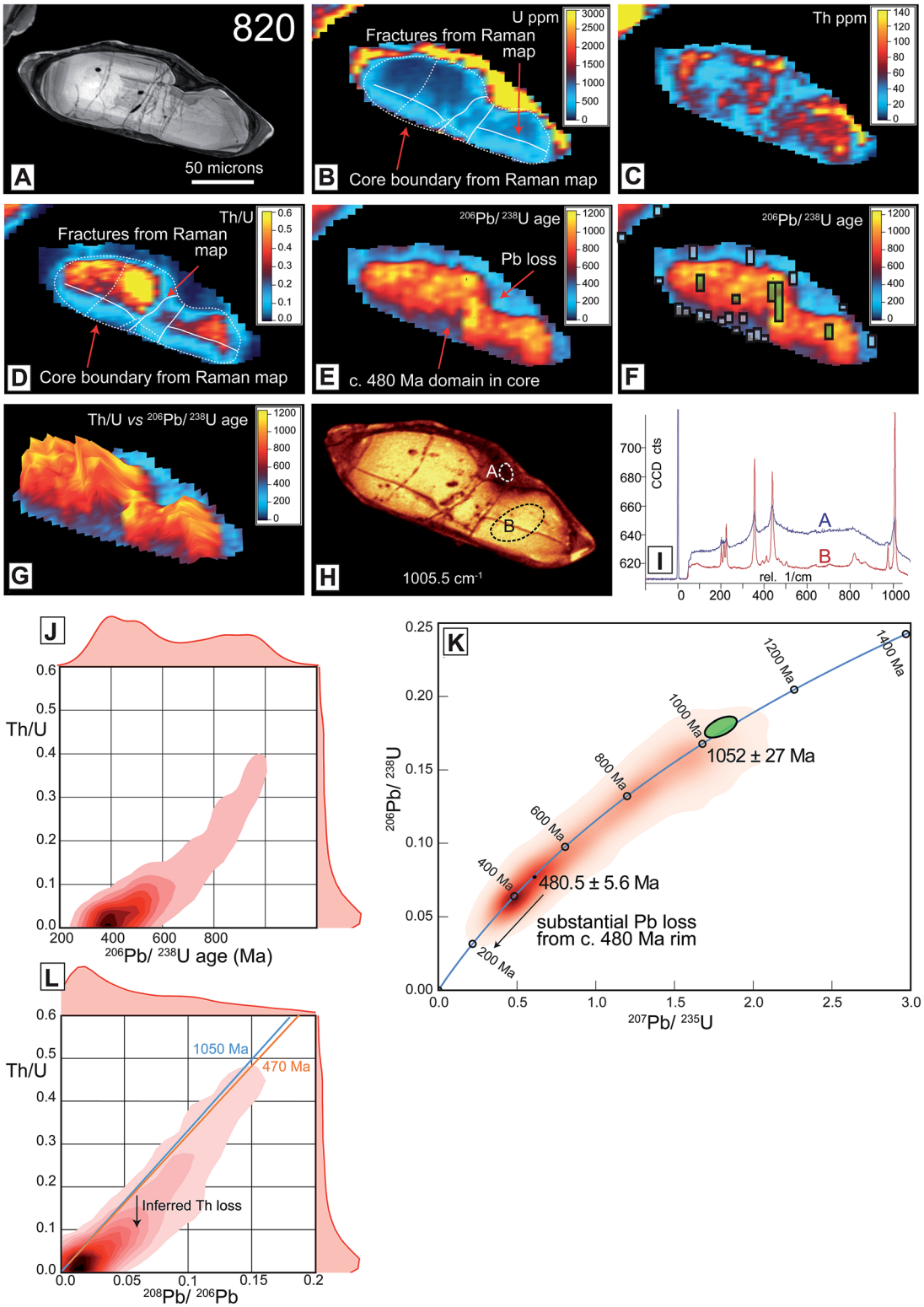

Fig. 5 Zircon 820 from leucocratic sheet sample DC 05/5-7. (A) CL image. (B–E) Agilent 7900 LA-ICPMS U ppm, Th ppm, Th/U ratio and $^{206}Pb/^{238}U$ image maps. (F) $^{206}Pb/^{238}U$ image map with concordant portions of the U/Pb signal denoted. (G) 3D map of $^{206}Pb/^{238}U$ age *vs.* Th/U ratio, with Th/U on the *z*-axis. (H) Raman peak intensity map at the 1005.5 cm^{-1} band. (I) Raman spectra of a representative metamict subdomain (trace A) and crystalline subdomain (trace B) from this sample. (J) Two-dimensional kernel density estimates of Th/U *vs.* $^{206}Pb/^{238}U$ age calculated from individual image data points. (K) Two-dimensional kernel density estimates from individual image data points plotted in the Wetherill concordia space. The concordia ages are calculated from the concordant portions of the U/Pb signal marked on (F). (L) Two-dimensional kernel density estimates of Th/U *vs.* $^{208}Pb/^{206}Pb$ calculated from individual image data points. 1050 Ma and 470 Ma reference lines of $^{208}Pb/^{206}Pb$ for a given Th/U ratio are illustrated.

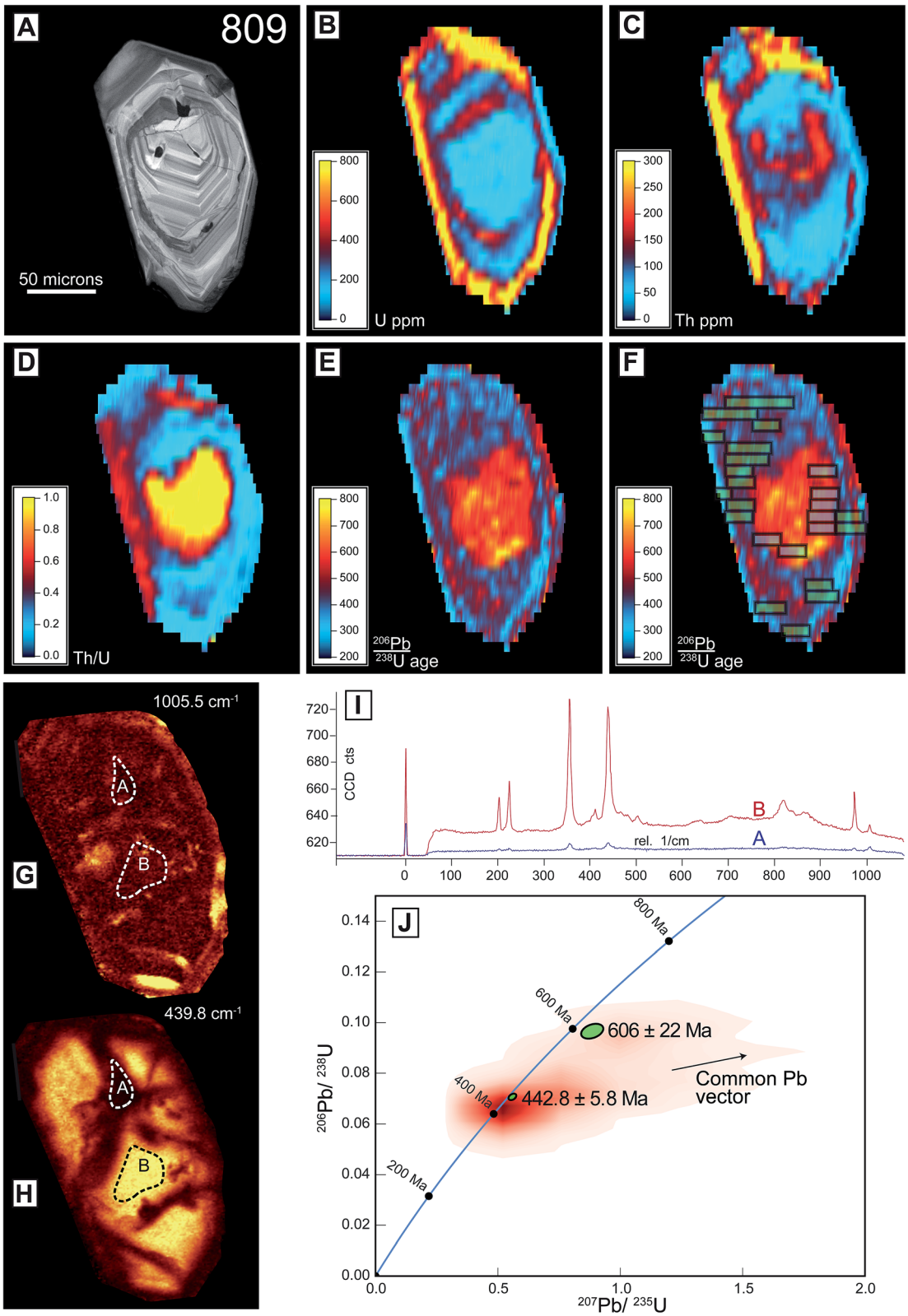

Fig. 6 Zircon 809 from syn-tectonic granitoid sample DC 04/5-2. (A) CL image. (B–E) Agilent 7900 LA-ICPMS U ppm, Th ppm, Th/U ratio and $^{206}Pb/^{238}U$ image maps. (F) $^{206}Pb/^{238}U$ image map with concordant portions of the U/Pb signal denoted. (G and H) Raman peak intensity maps at the 1005.5 cm^{-1} and 439.8 cm^{-1} bands. (I) Raman spectra of a representative metamict subdomain (trace A) and crystalline subdomain (trace B) from this sample. (J) Two-dimensional kernel density estimates from individual image data points plotted in the Wetherill concordia space. The concordia ages are calculated from the concordant portions of the U/Pb signal marked on (F).

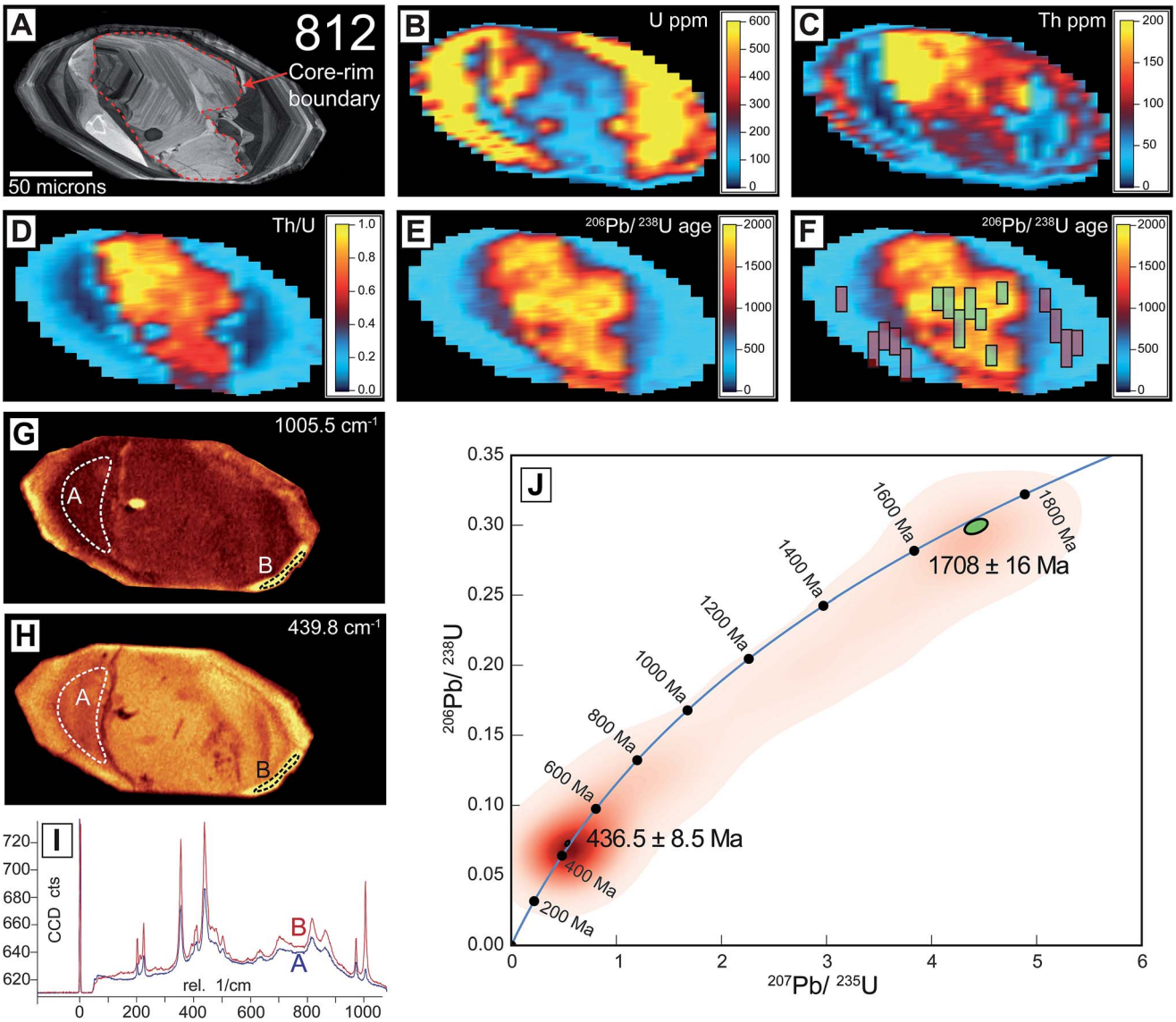

Fig. 7 Zircon 812 from syn-tectonic granitoid sample DC 04/5-2. (A) CL image. (B–E) Agilent 7900 LA-ICPMS U ppm, Th ppm, Th/U ratio and $^{206}Pb/^{238}U$ image maps. (F) $^{206}Pb/^{238}U$ image map with concordant portions of the U/Pb signal denoted. (G and H) Raman peak intensity maps at the 1005.5 cm^{-1} and 439.8 cm^{-1} bands. (I) Raman spectra of a representative metamict subdomain (trace A) and crystalline subdomain (trace B) from this sample. (J) Two-dimensional kernel density estimates from individual image data points plotted in the Wetherill concordia space. The concordia ages are calculated from the concordant portions of the U/Pb signal marked on (F).

characterised by extremely low Th/U ratios of *ca.* 0.02–0.05 (dark blue outer rim on Fig. 3D, 4D and 5D), while the outer portions of the core are typically characterised by Th/U ratios of *ca.* 0.1–0.2 (light blue zones on the same images).

Zircons from the syn-tectonic granitoid sample DC 04/5-2 (grains 809, 812, Fig. 6 and 7) exhibit a prominent oscillatory- and idiomorphic-zoned magmatic rim with a variable CL response, but which is typically darker than the oscillatory-zoned magmatic core. Similar to sample DC 05/5-7, there is a clear correlation between the CL images and LA-ICPMS U concentration maps (CL dark = high U; CL bright = low U). However, identifying core–rim structures from the U concentration maps alone is difficult, as the resolution is not sufficient to identify zoning truncation at the core–rim boundary, which is a key diagnostic feature on the CL maps (*e.g.* Fig. 6A and 7A). Similarly, while the Th/U ratio and Raman peak intensity maps help identify some portions of the core–rim boundary (particularly for sample 812, Fig. 7D and H), they too cannot unambiguously distinguish between the cores and the rims, which is presumably because both the inherited cores and rims share a magmatic origin.

Concordia systematics of individual samples

Zircon 823 from the leucocratic sheet sample DC 05/5-7 (Fig. 3) yields a core concordia age of 1133 ± 12 Ma and a rim concordia age of 477.0 ± 9.8 Ma (Fig. 3I). The Raman peak intensity map at the 1005.5 cm^{-1} band reveals a dark zone of metamict zircon (zone 'A' on Fig. 3G). The Raman spectrum of this rim

subdomain (trace 'A' on Fig. 3H) is characterised by a decrease in intensity and broadening of the ν_3 SiO_4 band at 1005 cm^{-1} compared to pristine crystalline zircon from the same sample (trace 'B' on Fig. 3H), with a similar effect observed for the bands at 973 cm^{-1}, 439 cm^{-1} and 355 cm^{-1}. This metamict zone contains up to 7500 ppm U. No concordant portions of signal could be detected across this U-rich portion of the rim and it exhibits significant Pb loss with $^{206}Pb/^{238}U$ ages as young as *ca.* 300 Ma (Fig. 3F). All concordant portions of the rim signal are characterised by extremely low Th/U values of *ca.* 0.02 (*cf.* Fig. 3D *vs.* F), including an embayment of low Th/U in the core, which is characterised by disturbed CL zoning (Fig. 3A). The oldest concordant portions of the core correlate with bright zones on Raman peak intensity map at the 1005.5 cm^{-1} band (*cf.* Fig. 3F *vs.* G) and the low U portions of the core (*cf.* Fig. 3F *vs.* B), but many portions of the core are substantially younger than the core concordia age of 1133 ± 12 Ma as evidenced by the cluster of data points ranging from *ca.* 1100 to 900 Ma on Fig. 3I. The discordia mixing line between the *ca.* 1100 Ma core and *ca.* 480 Ma rim indicated on Fig. 3I is thus a mixture of Pb loss from the *ca.* 1130 Ma core, with some additional minor mixing between the core and rim components. As the washout on the Analyte Excite – Agilent 7900 system is very fast, the latter mixing feature is attributed to the 7 μm laser spot sampling the core and rim simultaneously during the raster experiment.

Zircon 822 from the leucocratic sheet sample DC 05/5-7 (Fig. 4) yields a core concordia age of 1197 ± 12 Ma and a rim concordia age of 475.5 ± 3.9 Ma (Fig. 4J). The Raman peak intensity map at the 439.8 cm^{-1} band reveals darker zones of zircon (*e.g.* zone 'A' on Fig. 4G) on the U-rich rims, which are again characterised by a decrease in intensity and broadening of the 1005 cm^{-1}, 973 cm^{-1}, 439 cm^{-1} and 355 cm^{-1} bands (Fig. 4I). Even though these Raman-dark portions of the zircon rim contain up to 3000 ppm U (Fig. 4B), concordant portions of the U–Pb signal could be constructed across most of the rim without exhibiting Pb loss (Fig. 4F), with the two-dimensional kernel density estimates on the Wetherill concordia clustering around the *ca.* 1200 Ma core and the *ca.* 475 Ma rim (Fig. 4J).

Zircon 820 from the leucocratic sheet sample DC 05/5-7 (Fig. 5) exhibits similar concordia systematics to zircon 823 (Fig. 3). A dark zone of metamict zircon is visible on the Raman peak intensity map at the 1005.5 cm^{-1} band (zone 'A' on Fig. 5H). It contains up to 9000 ppm U, is characterised by a decrease in intensity and broadening of the 1005 cm^{-1}, 973 cm^{-1}, 439 cm^{-1} and 355 cm^{-1} bands (Fig. 5I), and exhibits substantial Pb loss (Fig. 5K). The oldest concordant portions of the core are associated with the highest Th//U ratios (Fig. 5J). This is supported by a 3D map of $^{206}Pb/^{238}U$ age *vs.* Th/U ratio, with Th/U on the *z*-axis (Fig. 5G). The highest elevations on the 3D map correspond to the largest Th/U ratios (*ca.* 0.4–0.5), and are clearly spatially associated with $^{206}Pb/^{238}U$ ages of *ca.* 1000 Ma and older (yellow-orange colours on Fig. 5G) along with U concentrations as low as 100 ppm (dark blue zones on Fig. 5B). However, the southern portion of the core (as inferred from Raman and CL textural evidence) yields a concordant *ca.* 480 Ma U–Pb age (subdomain highlighted on Fig. 3E), low Th/U ratios (*ca.* 0.1), U concentrations as high as 700 ppm, $^{232}Th–^{208}Pb$ ages > 2 Ga (not presented) and excess $^{208}Pb/^{206}Pb$ for a given Th/U ratio (Fig. 5L). The boundaries within the core between the young (*ca.* 480 Ma), low Th/U and the older (*ca.* 1050 Ma), high Th/U subdomains (Fig. 5B and D) correspond with prominent fractures identified on the Raman intensity map. These relationships imply that a *ca.* 1050 Ma core with magmatic Th/U ratios of *ca.* 0.4–0.5 has undergone variable U–Pb age resetting during leucocratic melt generation at 480 Ma. The resultant young domains on the outer core are characterised by low Th/U ratios of *ca.* 0.1, which are attributed to substantial loss at *ca.* 480 Ma of Th (as evidenced by the old $^{232}Th–^{208}Pb$ ages and unsupported ^{208}Pb) along intra-core fractures.

Zircons 809 and 812 from the syn-tectonic granitoid sample DC 04/5-2 (Fig. 6 and 7) are considered together. The Raman peak intensity map at the 439.8 cm^{-1} band reveals more internal structure than at the 1005.5 cm^{-1} band. In particular, darker zones of zircon on the Raman intensity map (*e.g.* zone 'A' on Fig. 6H) are visible in sample 809 and are characterised by a decrease in intensity and broadening of the 1005 cm^{-1}, 973 cm^{-1}, 439 cm^{-1} and 355 cm^{-1} bands (Fig. 6I), but do not correlate with the U distribution (Fig. 6B), and appear associated with fractures on the CL image (Fig. 6A). Core–rim structures which are clearly visible on the CL maps (*e.g.* Fig. 6A and 7A) cannot be unambiguously detected from the U concentration, Th/U ratio or Raman peak intensity maps, but do correlate well with the $^{206}Pb/^{238}U$ maps which clearly pick out the cores (Fig. 6F and 7F). Zircon 809 exhibits some Pb loss associated with high U zones (Fig. 6B), along with significant common Pb (Fig. 6J) which is present also on the iCAP Qc experiments and is not related to surface contamination. In contrast, the two-dimensional kernel density estimates on the Wetherill concordia for sample 812 cluster around the *ca.* 1700 Ma core and the *ca.* 435 Ma rim (Fig. 7J).

The weighted average age of the three concordia ages from the rims of grains 823, 822 and 820 from leucocratic sheet sample DC 05/5-7 is 477.1 ± 3.0 Ma (Table 3), which is within uncertainty of the U–Pb SIMS zircon concordia age of 477.9 ± 4.3 Ma.[15] The weighted average age of the two concordia ages from the rims of grains 809 and 812 from the syn-tectonic granitoid DC 04/5-2 sample is 440.8 ± 4.8 Ma (Table 3), which is within uncertainty of the U–Pb TIMS zircon concordia age of 442.4 ± 1.4 Ma for the *Sitabamba orthogneiss*.[15]

Discussion and conclusions

This study demonstrates that rapid LA-ICPMS U–Pb age maps (along with U and Th elemental concentration and Th/U ratio images) can be made on zircons with grain sizes typical of crystalline basement rocks in approximately 10 minutes. The protocol is easily modified for other LA-ICPMS systems. Key recommendations include extremely careful focusing and analysing several secondary zircon age standards, particularly during protocol development. Tuning the LA-ICPMS system on NIST 612 standard glass to yield Th/U ratios of unity, and an optimal choice of pulse energy (not too high yet comfortably above the ablation threshold for NIST612 glass and zircon) was

found to improve the age reproducibility of the secondary standards.

The laser scan speed employed is a function of the washout on the LA-ICPMS system. With the rapid washout on the Agilent 7900 system used in this study, scan speeds of 20 μm s^{-1} are possible without "blurring" of images. Once the laser scan speed has been set, the laser repetition rate is adjusted to yield rasters approximately one micron deep, while the mass spectrometer total duty cycle is adjusted to yield one sweep of the isotope list for every one micron of stage movement. Surficial common Pb contamination is removed by extremely careful cleaning of the mount prior to analysis, and can be augmented by firing a few laser pulses at a beam size larger than the entire zircon grain size (*e.g.* a 200 × 200 μm^2 square spot) as a rapid pre-ablation step. Employing raster areas only marginally larger than the zircon crystal boundaries can further reduce the total analysis time. In particular, extremely close packing of zircon crystals mounted in rows with their long axes parallel to each other is recommended. Rastering perpendicular to the zircon long axes would facilitate mapping two or three zircons in the same image, while not increasing the duration of the baseline measurements relative to a single zircon mapping experiment (baseline measurements can comprise nearly 50% of the mapping experiment duration for single zircons). However it should be noted that laser rasters running parallel to the crystal zonation (*e.g.* the high U upper rim on Fig. 5B) do not resolve features as clearly as laser rasters that run perpendicular to the crystal zonation. CL imaging prior to the mapping experiments should be used to guide the orientation of the raster scans relative to the zircon crystals.

The zircons from leucocratic sheet sample DC 05/5-7 (in particular grains 820 and 823) demonstrate clearly the potential applications of this technique. The LA-ICPMS imaging approach adopted here shows that the oldest concordant portions of the cores of grains 820 and 823 are associated with the highest Th/U ratios and lowest U contents, and are mantled by an outer portion of the core which is partially age reset and exhibits significantly lower Th/U ratios and higher U concentrations. U–Pb age resetting in the cores likely resulted from the higher U outer domain of the core having undergone Pb loss associated with metamictization. The low Th/U ratios restricted to the young, outer portions of the core clearly are bounded by intra-core fractures and yield evidence for Th loss, which may suggest reequilibration in the presence of the anatectic melt.

The partial age resetting described above does not clearly correlate with the CL imaging, and conventional LA-ICPMS (or SIMS) spot analyses in the cores of these complex polyphase zircons would result in a complex mixed age signal. Additionally, the significantly greater penetration depth of LA-ICPMS spot ablations (typically 10 to 20 μm) could result in complex mixed age signals which would be even harder to relate to the surface imaging. LA-ICPMS age mapping provides ample data directly relatable to other surface imaging techniques (combined with LA-ICPMS U and Th elemental concentration and Th/U ratio images) which makes the interpretation significantly more robust. Other elements (*e.g.* Fe, Sr, Li, REE, Hf), which may also yield additional petrological information, can easily be added to the analytical protocol. With an acquisition time of less than 10 minutes per map (which can potentially be decreased even further), there are few reasons to perform spot analyses on complex polyphase zircons other than when sensitivity is needed.

Acknowledgements

DC thanks Balz Kamber, Cora McKenna and Teresa Ubide for discussions with the LA-ICPMS imaging. NM thanks Georg Duesberg for access to Raman instrumentation. This material is partly based upon works supported by Science Foundation Ireland under Grant Numbers 12/IP/1663 and 15/IACA/3365 and an NSERC PDF awarded to JAP. Two anonymous reviewers are thanked for their comments that significantly improved the manuscript.

References

1 A. A. Nemchin and R. T. Pidgeon, *J. Petrol.*, 1997, **38**, 625–649.
2 M. J. Whitehouse and J. P. Platt, *Contrib. Mineral. Petrol.*, 2003, **145**, 61–74.
3 L. Nasdala, J. M. Hanchar, A. Kronz and M. J. Whitehouse, *Chem. Geol.*, 2005, **220**, 83–103.
4 S. M. Reddy, N. E. Timms, P. Trimby, P. D. Kinny, C. Buchan and K. Blake, *Geology*, 2006, **34**, 257–260.
5 J. Kramers, R. Frei, M. Newville, B. Kober and I. Villa, *Chem. Geol.*, 2009, **261**, 3–10.
6 U. Schaltegger, A. K. Schmitt and M. S. A. Horstwood, *Chem. Geol.*, 2015, **402**, 89–110.
7 J. J. Bellucci, M. J. Whitehouse, A. A. Nemchin, J. F. Snape, R. T. Pidgeon, M. Grange, S. M. Reddy and N. Timms, *Chem. Geol.*, 2016, **438**, 112–122.
8 M. A. Kusiak, M. J. Whitehouse, S. A. Wilde, A. A. Nemchin and C. Clark, *Geology*, 2013, **41**, 291–294.
9 J. W. Valley, A. J. Cavosie, T. Ushikubo, D. A. Reinhard, D. F. Lawrence, D. J. Larson, P. H. Clifton, T. F. Kelly, S. A. Wilde, D. E. Moser and M. J. Spicuzza, *Nat. Geosci.*, 2014, **7**, 219–223.
10 J. M. Cottle, M. S. A. Horstwood and R. R. Parrish, *J. Anal. At. Spectrom.*, 2009, **24**, 1355–1363.
11 J. M. Cottle, A. R. Kylander-Clark and J. C. Vrijmoed, *Chem. Geol.*, 2012, **332**, 136–147.
12 A. N. Steely, J. K. Hourigan and E. Juel, *Chem. Geol.*, 2014, **372**, 92–108.
13 L. Nasdala, A. Kronz, J. M. Hanchar, M. Tichomirowa, D. W. Davis and W. Hofmeister, *Am. Mineral.*, 2006, **91**, 1739–1746.
14 D. M. Chew, G. Pedemonte and E. Corbett, *Gondwana Res.*, 2016, **35**, 59–78.
15 D. M. Chew, U. Schaltegger, J. Košler, M. J. Whitehouse, M. Gutjahr, R. A. Spikings and A. Miškovic, *Geol. Soc. Am. Bull.*, 2007, **119**, 697–711.
16 D. M. Chew, U. Schaltegger, A. Miškovic, D. Fontignie and M. Frank, in *6th International Symposium on Andean Geodynamics (ISAG 2005, Barcelona), Extended Abstracts*, 2005, pp. 166–169.

17 D. M. Chew, J. A. Petrus and B. S. Kamber, *Chem. Geol.*, 2014, **363**, 195–199.
18 C. C. Garcia, H. Lindner and K. Niemax, *J. Anal. At. Spectrom.*, 2009, **24**, 14–26.
19 J. Woodhead, J. Hergt, M. Shelley, S. Eggins and R. Kemp, *Chem. Geol.*, 2004, **209**, 121–135.
20 T. Ubide, C. A. McKenna, D. M. Chew and B. S. Kamber, *Chem. Geol.*, 2015, **409**, 157–168.
21 M. Wiedenbeck, P. Alle, F. Corfu, W. L. Griffin, M. Meier, F. Oberli, A. von Quadt, J. C. Roddick and W. Spiegel, *Geostand. Newsl.*, 1995, **19**, 1–23.
22 M. Wiedenbeck, J. M. Hanchar, W. H. Peck, P. Sylvester, J. Valley, M. Whitehouse, A. Kronz, Y. Morishita, L. Nasdala, J. Fiebig, I. Franchi, J. P. Girard, R. C. Greenwood, R. Hinton, N. Kita, P. R. D. Mason, M. Norman, M. Ogasawara, R. Piccoli, D. Rhede, H. Satoh, B. Schulz-Dobrick, O. Skar, M. J. Spicuzza, K. Terada, A. Tindle, S. Togashi, T. Vennemann, Q. Xie and Y. F. Zheng, *Geostand. Geoanal. Res.*, 2004, **28**, 9–39.
23 L. P. Black, S. L. Kamo, C. M. Allen, J. N. Aleinikoff, D. W. Davis, R. J. Korsch and C. Foudoulis, *Chem. Geol.*, 2003, **200**, 155–170.
24 J. Slama, J. Košler, D. J. Condon, J. L. Crowley, A. Gerdes, J. M. Hanchar, M. S. A. Horstwood, G. A. Morris, L. Nasdala, N. Norberg, U. Schaltegger, B. Schoene, M. N. Tubrett and M. J. Whitehouse, *Chem. Geol.*, 2008, **249**, 1–35.
25 M. A. Pointon, R. A. Cliff and D. M. Chew, *Geol. J.*, 2012, **47**, 77–98.
26 J. B. Paces and J. D. Miller, *J. Geophys. Res.: Space Phys.*, 1993, **98**, 13997.
27 O. Bachmann, F. Oberli, M. A. Dungan, M. Meier, R. Mundil and H. Fischer, *Chem. Geol.*, 2007, **236**, 134–166.
28 M. Ganerød, D. M. Chew, M. A. Smethurst, V. R. Troll, F. Corfu, F. Meade and T. Prestvik, *Chem. Geol.*, 2011, **286**, 222–228.
29 C. Paton, J. Hellstrom, B. Paul, J. Woodhead and J. Hergt, *J. Anal. At. Spectrom.*, 2011, **26**, 2508–2518.
30 J. A. Petrus and B. S. Kamber, *Geostand. Geoanal. Res.*, 2012, **36**, 247–270.
31 C. Paton, J. D. Woodhead, J. C. Hellstrom, J. M. Hergt, A. Greig and R. Maas, *Geochem., Geophys., Geosyst.*, 2010, **11**.
32 K. R. Ludwig, *User's manual for a geochronological toolkit for Microsoft Excel (Isoplot/Ex version 3.0)*, Berkeley Geochronol. Cent. Spec. Publ., 2003, vol. 4, pp. 1–70.
33 D. W. Scott, *Multivariate Density Estimation: Theory, Practice, and Visualization*, Wiley-Interscience, 1992.